Long-duration blast loading & response of steel column sections at different angles of incidence

Jack W. Denny[a,*], Simon K. Clubley[b]

[a] Faculty of Engineering and Physical Sciences, University of Southampton, SO17 1BJ, United Kingdom
[b] School of Architecture, Building and Civil Engineering, Loughborough University, LE11 3TU, United Kingdom

ABSTRACT

This paper reports experimental results pertaining to the effects of planar long-duration blast waves interacting with steel I-section column elements about different angles of incidence. Long-duration blast waves are typically defined by a positive pressure phase duration in excess of 100 ms, characteristic of very large explosion events such as industrial accidents. Blasts of this magnitude result in large impulses and dynamic pressures with the potential to exert high drag forces on column elements within an open frame structure. Due to relatively small dimensions in comparison to the blast wavelength, individual column elements are predominantly subjected to translational drag loading. Blast drag loading is complex to characterise, generally requiring approximation using drag coefficients, although proposed values in literature display inconsistency and typically lack provision for multi-axis interaction with I-shape geometries. Four full-scale long-duration experiments investigated blast interaction and elastic structural response of two steel I-section columns as a function of orientation to the incident shock wave. Drag coefficients were calculated as a function of I-section orientation using experimental pressure data and compared to values proposed in literature. It was found that drag coefficients proposed in literature have the potential to under-predict drag loading for certain oblique I-section orientations examined in these experiments. Importantly, intermediate oblique I-section orientations recorded higher loading and exhibited higher drag coefficients compared to orthogonal orientations, resulting in larger structural elastic response. Results from this experimental work have confirmed that I-section columns are axis-sensitive to blast wave direction giving rise to varying magnitudes of drag loading and structural response.

1. Introduction

This paper reports on experimental results investigating the effects of long-duration blast loading on steel I-section column elements. Steel columns are found extensively in the construction of single to multi-storey framed structures. Explosive blast loading has the potential to exert forces on steel columns far higher than their capacity, causing permanent deformation. A number of recent large-scale industrial accidents such as the 2005 Buncefield and 2009 Jaipur oil refinery disasters, the 2013 West Texas fertiliser factory explosion and the 2015 Tianjin disaster highlight a growing need to understand the response of structures to long-duration blasts.

Long-duration blast waves are typically defined by positive pressure durations over 100 ms, which develop in later stages of shock wave propagation i.e. in the 'far field' from the source of detonation. Blast waves reaching this later stage of propagation with sufficient energy to cause structural damage are characteristic of very large-scale explosive

events. In the modern world, these are most commonly caused by hydrocarbon vapour cloud explosions (VCE) at petrochemical facilities due to the nature in which volatile hydrocarbons are stored, equating to large amounts of potential energy. Notable recent examples include the 2005 'Buncefield Disaster', which exhibited an estimated TNT equivalence of 105–250 T TNT [1,2]. This caused damage to steel frame structures over a wide area and in many cases, the buildings had to be demolished or abandoned for prolonged time periods [3]. Other causes include the detonation of volatile industrial chemicals, particularly at processing and storage facilities. For example, the 2013 West Texas fertiliser plant explosion in which a fire caused the detonation of ~30 T of ammonium nitrate causing a blast with an estimated 12.5 T TNT equivalence [4]. Approximately 150 buildings were damaged within a 4 km radius, the cost of which was estimated to exceed $100 million, 15 people were killed and ~160 injured [5].

Long-duration blasts are extremely powerful, generating substantial impulse and dynamic pressures that considerably exceed short-duration

---

* Corresponding author.
  E-mail addresses: Jack.Denny@soton.ac.uk (J.W. Denny), S.Clubley@lboro.ac.uk (S.K. Clubley).

Fig. 1. The Air Blast Tunnel (ABT), MOD Shoeburyness, UK (Clubley, 2013).

blasts of the same peak overpressure. Importantly, long pressure durations enable greater kinetic mobilisation of air particles behind the blast front, thereby generating dynamic pressures (blast winds) capable of exerting significant drag loads on slender structural elements such as columns. Long-duration blasts are therefore far more destructive and particularly damaging to open frame structures and constituent column elements.

In reality, structures and their constituent column elements may be subjected to blast waves from various angles of incidence (multi-axis interaction) depending on the location of detonation. Such multi-axis blast loading scenarios may arise in industrial operations where volatile, explosive materials are confined to certain areas of a facility. Structural damage and debris analysis after the 1945 bombings of Hiroshima and Nagasaki found that identical adjacent steel warehouses exhibited different damage states due to their orientation with respect to the blast, thus highlighting sensitivity to multi-axis blast loading [6]. An understanding of multi-axis blast loading behaviour is important when designing security perimeters as it may be necessary to limit structural columns from blast exposure at known sensitive axes.

Correctly characterising blast loading exerted on column elements is essential for deriving reliable structural response solutions. When long-duration blasts act on individual column elements, the diffraction loading phase is reduced to a short-duration initial spike as the blast envelops the column, followed by loading due to flow of the displaced air i.e. drag loading. This is due to rapid equalisation of blast over-pressures associated with the small column dimensions in comparison to blast wavelength. Individual column elements are therefore considered 'drag-sensitive' where translational drag loading from the dynamic pressures or 'blast wind' have predominant effect.

Characterising time varying blast loads on respective surfaces of an intricate I-section geometry can be complex, particularly when considering different angles of incidence in the case of multi-axis interaction. Drag loading depends on section geometry and orientation and is directly proportional to the dynamic pressure regime. The density and viscosity of the air flowing around the section has a direct effect on the drag forces exerted in conjunction with complex aerodynamic and boundary layer effects such as flow separation and wake. Given this complexity, engineers tend to simplify and expedite the calculation of translational drag loading on a structure by employing drag coefficients, which attempt to encapsulate all these factors within a single modifier. In the majority of cases, drag coefficients are case dependent and determined experimentally. Drag coefficients provide a quick method of calculating the translational net drag load acting on a structure with a certain geometry and orientation to the blast without the need to model complex aerodynamic processes occurring at a local scale.

The concept of modifying the product of dynamic pressure and projected area by a dimensionless drag coefficient C_D has been universally adopted in blast literature [7–10]. The drag force, $F_X(t)$ exerted on an object with respect to time is related to the incident dynamic pressure q(t) (blast wind), the projected area of the object normal to the blast wind direction (X), A_X and the drag coefficient, C_D (Eq. (1)).

$$F_X(t) = C_D. A_X. q(t) \tag{1}$$

While there has been considerable prior research into characterising clearing and blast interaction with finite structures and columns [11–13], these studies concentrate on short-duration blasts for which drag loading is relatively inconsequential. As a result, the prevalence of blast drag coefficients pertinent to I-sections in open literature is very limited, particularly when considering different section orientations. Glasstone and Dolan [14] or Hoerner [15] suggest inconsistent values of $C_D = 1.5$ and $C_D = 2.05$ respectively for 'sharp edged sections' although no guidance towards the orientation for which these values are applicable is provided. Blackmore [16] suggests a value of $C_D = 2.0$ for all common sharp edged channel sections including I-sections. The Australian & New Zealand Standards for Wind Actions [17] propose drag force coefficients of $C_D = 1.9$ and $C_D = 1.6$ for exposed structural I-sections at orientations of 0 and 90° respectively.

Overall, proposed drag coefficients in literature demonstrate inconsistency and are typically single values that lack provision for different angles of incidence; therefore it is simply unknown how to characterise drag loading for oblique, intermediate column section orientations. Furthermore, no prior experimental studies have investigated the effects of column section orientation on blast loading when subjected to long-duration blast. This paper presents experimental findings that examine and quantify the influence of multi-axis blast interaction on the loading and structural response of steel I-section columns as a function of orientation.

2. Experimental methodology

Long-duration blast waves were generated using the national Air Blast Tunnel (ABT) facility at MoD Shoeburyness, UK. Constructed in 1964, the ABT is one of very few facilities in the world capable of examining the structural response to long-duration blast waves (Fig. 1). At approximately 200 m long in total, the tunnel has two main test sections: a 4.9 m diameter section and 10.2 m diameter section. The ABT is capable of generating blast waves with long-duration characteristics; a peak overpressure of $p_i \approx 55$ kPa and positive phase duration of $t^+ \approx 155$ ms are attainable at maximum power in the 10.2 m section. This pressure regime differs greatly in comparison to the shorter durations of 10–20 ms, typical of arena HE detonations. A driver charge is located in a 1.8 m diameter section and the long increasing diameter of the tunnel effectively re-shapes the blast into a substantially longer wavelength with characteristics of a near-planar long-duration, Mach stem pulse. The rear entrance of the tunnel is equipped with a rarefaction wave eliminator (RWE) which assists in the reduction of unwanted reflections in the upstream direction (Figs. 1 and 5). For each experiment, blast waves with consistent parameters were sought at maximum power inside the 10.2 m section. Through re-shaping the

Table 1
Blast trials schedule.

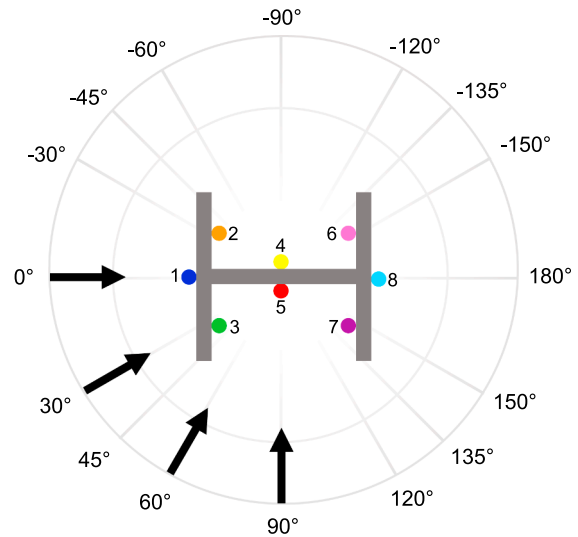| Trial	ABT location	Incident peak overpressure, p_i (kPa)	Total incident impulse, I_i (kPa ms)	I-Section orientation	
				Specimen A UKC 152 × 152 × 23	Specimen B UKC 203 × 203 × 46
1	10.2 m	55	3380	0°	0°
2	10.2 m	55	3380	30°	30°
3	10.2 m	55	3380	60°	60°
4	10.2 m	55	3380	90°	90°

propagating shock wave, a blast is achieved with TNT equivalence of approximately 250 T at a 200 m stand-off distance when calculated via the Kingery and Bulmash predictive polynomial equations [18].

Four full-scale long-duration blast trials were conducted using the ABT to investigate and quantify the influence of multi-axis blast interaction on the loading and structural dynamic response of two steel I-section columns (Table 1). Multi-axis blast loading was investigated by aligning both column specimens at different orientations to the experimental blast propagation inside the ABT. Each trial utilised two 3.00 m height columns, including two variations of I-section that were subjected to four successive blasts at section orientations of 0, 30, 60 and 90° (Table 2, Fig. 2). Both columns were designed to respond elastically to the blast loading conditions to allow repeat firings of the sections about different orientations. Each column was fixed to the ground in a cantilever configuration to generate the greatest flexural structural response in the blast environment (Fig. 3). Specimen A (UKC 203 × 203 × 46) was designed to exhibit minimal mechanical response and was instrumented with eight Endevco 8515C-50 pressure transducers. These were secured to the centre point of each cross-section surface at mid-height to measure blast flow interaction and pressures exerted on each column surface (Figs. 2 and 6). Specimen B (UKC 152 × 152 × 23) was designed to produce increased elastic response to examine structural response as a function of section orientation. Both columns were fixed at the base using a bespoke adjustable base plate design providing a fully-fixed support that allowed the section to be rotated in-situ between trials to achieve the specified orientations (Fig. 4).

The incident blast environment was measured by instrumenting two locations adjacent to both column specimens at a distance of 2.0 m (Fig. 5). Endevco 8510-50 static overpressure gauges and Kulite-20D dynamic pressure gauges were employed to record peak pressures, specific impulse and positive phase durations for the free-field environment. Dual instrumentation either side of the column assemblies provided redundancy and the ability to monitor blast wave uniformity at two lateral positions across the 10.2 m ABT section. High-speed Phantom cameras were used to record column deflection-time histories at 2000 fps with 800 × 600 resolutions. Two cameras were aligned with the more responsive Specimen B from two elevation perspectives and one from the side of Specimen A (Fig. 5). LEDs were positioned within the column assembly to signal blast wave arrival via pressure-triggered illumination, aiding subsequent high-speed video analysis of the column deflection-time histories.

Fig. 2. Multi-axis blast loading angle and surface pressure gauge numbering convention.

3. Results and discussion

Static overpressure and dynamic pressures were recorded inside the ABT at 'left' and 'right' locations (Fig. 5) 2.00 m adjacent to the column assemblies to assess the incident blast environment and trial repeatability. Particular consideration was given to pressure data recorded at the left location gauges as these were adjacent to Specimen A (UKC 203 × 203 × 46) that was instrumented with surface pressure transducers.

Recorded static and dynamic pressure-time histories were characteristic of an ideal blast wave type i.e. a Friedlander decay curve was observed although some non-ideal discontinuities were observed throughout the positive phase duration (Fig. 7a and b). This occurred for all four trials and can also be seen in archival pressure data for the ABT operating at maximum power, suggesting that this pattern is characteristic of the ABT facility [19,20].

Overall, static overpressures recorded over the four trials at both gauge locations demonstrated good agreement and successfully represented the design blast conditions. A mean peak incident static overpressure value of $p_i = 58.7$ kPa was recorded at both gauge locations (left and right) across the four trials (Table 3). Mean positive phase durations of $t^+ = 154.3$ ms and 158.8 ms were recorded at the left and right gauge locations respectively. Mean positive phase total impulses of $I_i = 3370$ kPa ms and $I_i = 3420$ kPa ms were recorded at the left and right locations respectively (Table 3). The right gauge PI(R) recorded moderately larger positive phase durations ($\Delta t^+ = 4.5$ ms) and impulses ($\Delta I_i = 50$ kPa ms) on average although the assumption of a planar blast wave is acceptable due to these relatively small differences (Table 3). At the left gauge location, standard deviations for incident static overpressure and total impulse were small across the four trials with values representing only 0.46% and 0.75% of the mean

Table 2
I-section column specimen properties.

	Specimen A	Specimen B
Column section	UKC 203 × 203 × 46	UKC 152 × 152 × 23
Experimental concept	8 Surface-mounted pressure transducers measure multi-axis blast interaction	Smaller section designed for measurable elastic structural response
Steel grade	S275	S275
Second moment of area (cm^4)	$I_{yy} = 4568$	$I_{yy} = 1250$
	$I_{zz} = 1548$	$I_{zz} = 400$
Column total height (mm)	3000	3000

Fig. 3. Trial configuration in the ABT viewed downstream for the 0° I-section orientation (Trial 1).

respectively, indicating a well-replicated, consistent blast environment (Table 5a).

Dynamic pressure data also exhibited good agreement, although with greater variability. Peak dynamic pressure values recorded at both gauge locations demonstrated good consistency over the four trials with mean values of 9.0 and 8.9 at gauges PD(L) and PD(R) respectively (Table 4). Peak dynamic pressures recorded at the left gauge display small standard deviation values representing 0.92% of the mean across the four trials (Table 5b). Positive phase duration and impulse recorded at the left and right sides of the ABT generally demonstrated less agreement than static overpressure measurements. This is caused by the unavoidable level of vorticity and turbulence existing behind the highly compressed air at the planar shock front, and thus blast winds are more susceptible to varying spatially and temporally within the ABT facility. A mean dynamic impulse of $I_q = 463$ kPa ms was calculated at the left gauge, PD(L) with a standard deviation equivalent to 4.26% of the mean (Table 5b). This shows that a higher degree of variance occurred throughout the four trials, indicating that dynamic pressures behind the shockwave are more difficult to control under experimental conditions. Overall, the incident blast environment demonstrated good repeatability and it is acceptable to assume both columns were subjected to effectively consistent incident blast conditions.

3.1. Multi-axis blast loading

For each I-section orientation tested, eight pressure transducers on Specimen A (UKC 203 × 203 × 46) recorded pressure-time histories at the centre point of respective cross section surfaces. With a higher elastic section modulus, Specimen A exhibited negligible structural response for each I-section orientation tested, verified by inspection of high-speed video footage. It can therefore be assumed that mechanical

response did not influence blast interaction or loading exerted on Specimen A i.e. Fluid-structure interaction (FSI) effects can be neglected. Analysis of pressure-time histories quantified respective surface impulses and calculation of the net translational loading exerted on the entire column as a function of I-section orientation to the blast. Total impulses on each surface were calculated by integrating respective pressure-time histories over the positive phase duration and plotted as a function of I-section orientation in Fig. 8 with incident total impulse overlaid for reference. Total surface impulses quantify the blast energy transferred to respective surfaces, providing insight into blast drag loading behaviour from different angles of incidence.

Surface impulses vary considerably with I-section orientation to the blast (Fig. 8), influenced by both relative exposure of a particular surface to the blast and the presence of aerodynamic effects. Exposed surfaces exhibited the highest impulses; a maximum value was observed for the front flange (surface 1) at the 0° orientation and surfaces 3, 5 and 7 at the 90° orientation shown in Fig. 8. In these cases, exposed surfaces experienced a total impulse exceeding the free-field incident impulse (Fig. 8). For less exposed or 'shielded' surfaces, total impulses fall below the incident value (Fig. 8). Surfaces 2, 4, 6 and 8 are comparably shielded throughout orientations 0–90° with total impulse values consistently below that of the incident blast wave (Fig. 8). Collectively, these four shielded surfaces experienced minimum impulse at the 30° orientation (Fig. 8), approximately 500 kPa ms less than the free-field. This indicates a high degree of shielding where aerodynamic effects such as flow separation, regions of wake and vorticity manifest as reduced stagnation pressures on these surfaces. At an orientation of 60°, the impulse exerted on the rear-facing flange (surface 8) continues to decrease to a minimum value whilst the shielded surfaces' (2, 4 and 6) impulse gradually increases indicating reduced shielding effects at this angle. At the 90° orientation, surface 2, 4 and 6 impulses continue
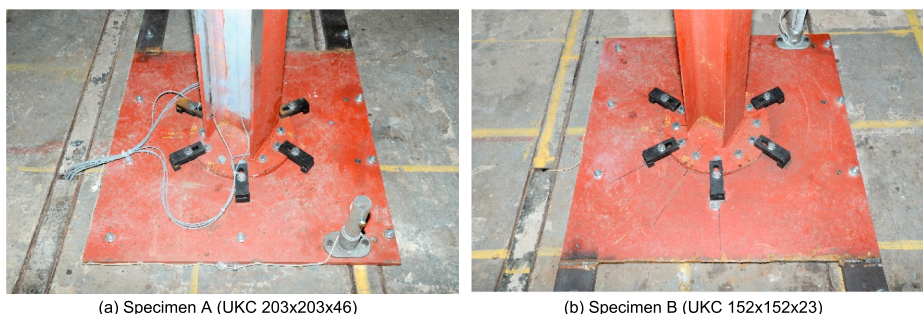

(a) Specimen A (UKC 203x203x46)   (b) Specimen B (UKC 152x152x23)

Fig. 4. Circular base plate design enabling 30° I-section orientation to the blast (Trial 2).
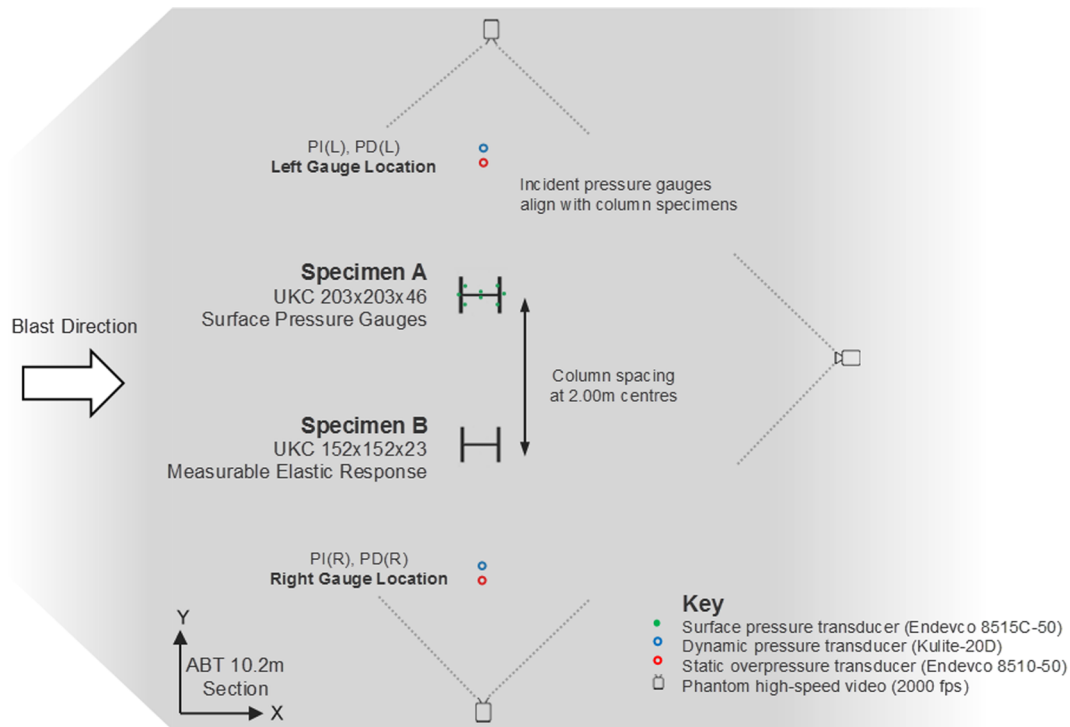
Fig. 5. Plan view schematic of the trial configuration for the 0° I-section orientation (Trial 1).

Fig. 6. Endevco 8515C-50 surface pressure transducers mounted on Specimen A.

to increase to the order of 3210–3260 kPa ms, comparable to the incident impulse (3389 kPa ms). These relatively higher impulse values demonstrate that despite being unexposed to the blast, reduced aerodynamic effects enable larger stagnation pressures to load these rear surfaces. Analysis has therefore shown that respective surface impulses are greatly influenced by both relative exposure to the blast wave and the aerodynamic interaction with the section geometry features.

Net force-time histories exerted on the entire column were calculated as a function of I-section orientation by multiplying respective surface pressure-time histories by their corresponding projected areas and resolved in the blast X-direction. As drag loading is predominant, net pressures exerted on the column surfaces are resolved in the blast X-direction (consistent with the transient blast winds) for each I-section orientation. Net force-time histories take account of respective I-section surface projected areas at each orientation and represent the resultant

total loading with respect to time, $F_X(t)$ exerted on the column in the blast X-direction (Fig. 9). These net force-time histories were also integrated with respect to time over the positive phase duration to calculate the cumulative and total net impulse, I_X exerted on the column as a function of I-section orientation (Fig. 9).

Peak instantaneous forces on the column at each orientation exhibited similar values representing the rapid blast diffraction stage, although subsequent drag loading varied in magnitude (Fig. 9). Higher transient drag loading was exerted on the column at orientations of 30° and 60° to the blast, as visible in the net force-time plots in Fig. 9b and c. Cumulative net impulse-time curves are replotted and overlaid in Fig. 10b to allow comparison of the rate of loading as a function of I-section orientation. Gradients of the cumulative impulse curves are comparably steeper for the 30° and 60° I-section orientations, indicating a higher rate of loading at these orientations (Fig. 10b).

Total net impulse, I_X accumulated over the positive phase duration is displayed as a function of section orientation in Fig. 10a. Similar net blast loading was exerted on the column at the orthogonal 0° and 90° orientations with total impulses of 415 kN ms and 423 kN ms respectively (Fig. 10a). With comparable projected areas, blast loading exerted on the I-section at these two orientations appears to be relatively equivalent suggesting they have similar blast aerodynamic properties. Noticeably higher loading was exerted on the I-section at the oblique orientations of 30° and 60° however, demonstrated by higher total impulses, I_X and steeper cumulative impulse gradients (Fig. 10). Maximum I-section loading occurred at the 60° orientation with a total impulse of $I_X = 662$ kN ms, 60% and 56% higher than the column orientated at 0° and 90° respectively (Fig. 10a).

The second highest loading occurred at the 30° orientation with a total impulse of $I_X = 567$ kN ms and steep cumulative impulse gradient, slightly less than the column orientated at 60°. The 30° column orientation resulted in 36% higher total net impulse than at 0° which can be attributed to the section's increased projected area to the blast, which also increases by 36%. The 60° orientation resulted in higher loading than at 30° with a total impulse 17% higher ($I_X = 662$ kN ms) and increased rate of loading (steeper cumulative impulse gradient) despite having the same projected area. With consideration of
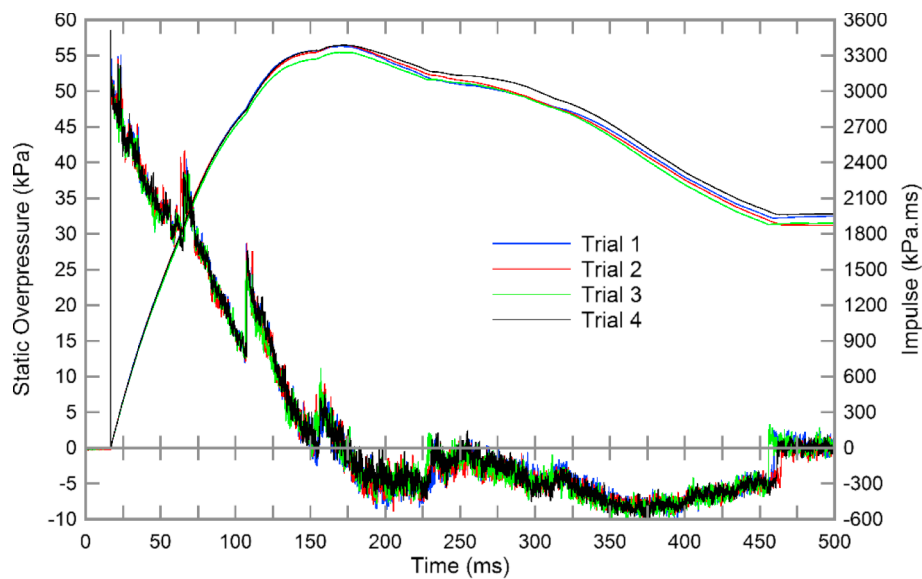
a) Static overpressure-time histories (Trials 1-4).
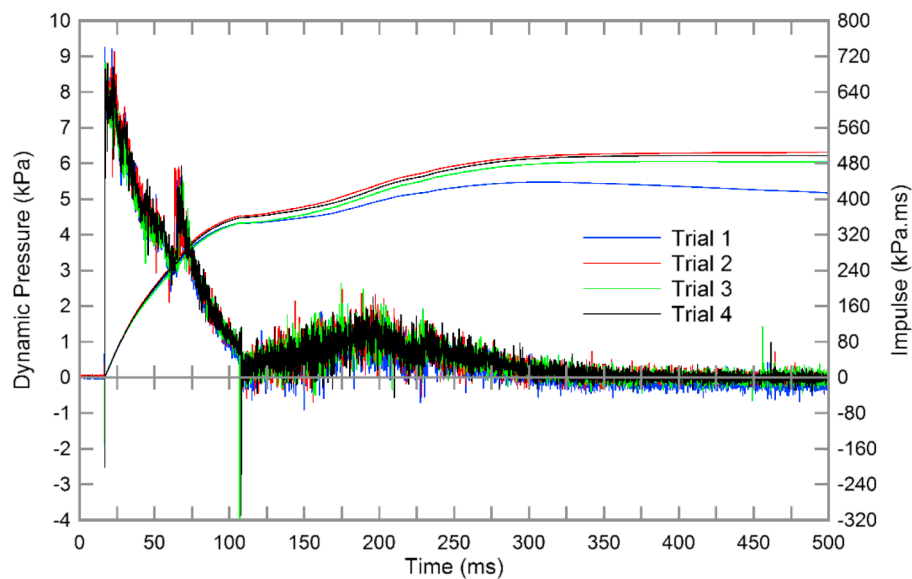
(b) Dynamic pressure-time histories (Trials 1-4).

Fig. 7. Incident static overpressure (a) and dynamic pressure (b) time histories and cumulative impulse recorded at left gauge location.

Table 3
Incident blast environment – static overpressure parameters.

(a) Left gauge location, PI(L)

Incident blast overpressure parameters	Trial 1	Trial 2	Trial 3	Trial 4	Mean
Peak incident overpressure, p_i (kPa)	59.1	58.4	58.6	58.5	58.7
Positive phase duration, t^+ (ms)	154.2	154.8	152.6	155.6	154.3
Positive phase incident impulse, I_i (kPa ms)	3377	3387	3327	3389	3370

(b) Right gauge location, PI(R)

Incident blast overpressure parameters	Trial 1	Trial 2	Trial 3	Trial 4	Mean
Peak incident overpressure, p_i (kPa)	59.1	58.7	58.7	58.3	58.7
Positive phase duration, t^+ (ms)	153.1	159.5	162.0	160.7	158.8
Positive phase incident impulse, I_i (kPa ms)	3440	3454	3360	3427	3420

Table 4
Incident blast environment – dynamic pressure parameters.

(a) Left gauge location, PD(L)

Incident dynamic pressure parameters	Trial 1	Trial 2	Trial 3	Trial 4	Mean
Peak dynamic pressure, q (kPa)	9.1	9.0	9.1	8.9	9.0
Positive phase duration, t_q^+ (ms)	286.1	337.2	305.9	339.0	317.1.0
Positive phase dynamic impulse, I_q (kPa ms)	438	484	450	480	463

(b) Right gauge location, PD(R)

Incident dynamic pressure parameters	Trial 1	Trial 2	Trial 3	Trial 4	Mean
Peak dynamic pressure, q (kPa)	9.1	8.8	9.0	8.8	8.9
Positive phase duration, t_q^+ (ms)	337.8	348.4	316.0	343.1	336.3
Positive phase dynamic impulse, I_q (kPa ms)	476	483	470	493	481

Table 5
Incident blast wave variation through trials 1–4 at left gauge location.

(a) Static overpressure – left gauge location, PI(L)

Trials	Gauge	Mean values ($\bar{X}$)			Standard deviation (σ)					
		p_i (kPa)	t^+ (ms)	I_i (kPa ms)	p_i (kPa)	t^+ (ms)	I_i (kPa ms)	p_i (% of $\bar{X}$)	t^+ (% of $\bar{X}$)	I_i (% of $\bar{X}$)
1–4	PI(L)	58.7	154.3	3370	0.3	1.093	25.3	0.46%	0.71%	0.75%

(b) Dynamic pressure – left gauge location, PD(L)

Trials	Gauge	Mean values ($\bar{X}$)			Standard deviation (σ)					
		q (kPa)	t_q^+ (ms)	I_q (kPa ms)	q (kPa)	t_q^+ (ms)	I_q (kPa ms)	q (% of $\bar{X}$)	t_q^+ (% of $\bar{X}$)	I_q (% of $\bar{X}$)
1–4	PD(L)	9.0	317.1	463	0.1	22.2	19.7	0.92%	7.00%	4.26%

individual surface impulses, higher loading at the 60° orientation can be attributed to lower restoring impulse on the rear sheltered surfaces, associated with a high degree of shielding at this orientation (Fig. 8). Effectively, the geometry features at 60° causes the rear web (surface 4) to attain a much lower impulse than the exposed web (surface 5), thus generating relatively high net loading (Fig. 8). The 60° I-section orientation is therefore more bluff than the other orientations, generating higher drag loading.

The non-symmetrical variation in total impulse as a function of I-section orientation demonstrates that column section aerodynamics are non-trivial and net loading is not simply a function of column projected area to the blast (Fig. 10). These experimental results and analysis confirm that I-section orientation with respect to the blast (i.e. multi-axis interaction) has noticeable influence on net total loading exerted on a column. Oblique orientations generated higher blast loading partly due to increased projected area, but also due to varying aerodynamics, providing reason to calculate drag coefficients.

Using experimental surface pressure data, drag coefficients were calculated for the UKC 203 × 203 × 46 I-section as a function of the orientations tested. Integrating the drag force equation with respect to time (Eq. (2)) for the positive phase duration ($t = t_a + t^+$) results in an expression relating the dynamic impulse, I_q, projected area, A_X and drag coefficient, C_D with the net total impulse exerted on the structure in the blast X-direction, I_X (Eq. (3)). The drag force impulse, I_X represents the net total impulses exerted on the entire column calculated using surface pressure-time histories (Fig. 10a).

$$\int_{t=t_a}^{t=t_a+t^+} F_X(t)dt = C_D . A_X . \int_{t=t_a}^{t=t_a+t^+} q(t)dt \qquad (2)$$

$$I_X = C_D . A_X . I_q \qquad (3)$$

Rearranging Eq. (3) produces an expression for the effective drag coefficient of the column, applicable to the I-section in the blast X-direction:
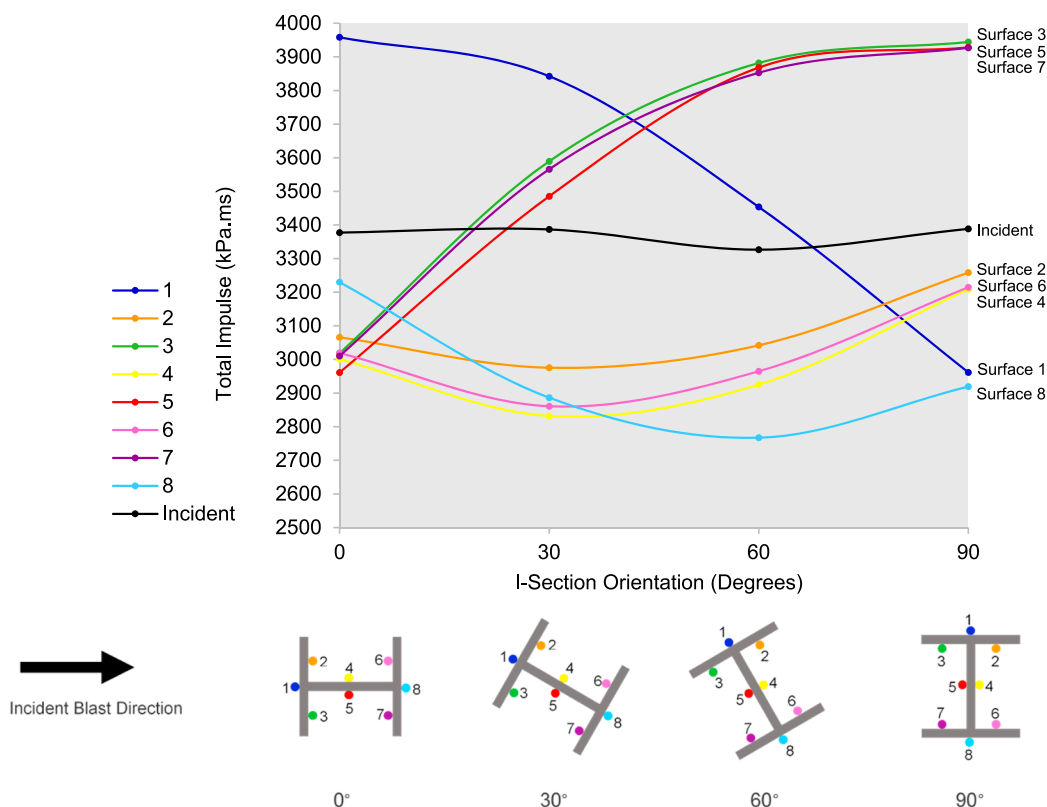
$$C_D = \frac{I_X}{A_X . I_q} \qquad (4)$$

Fig. 8. Surface total impulse variation with I-section orientation.
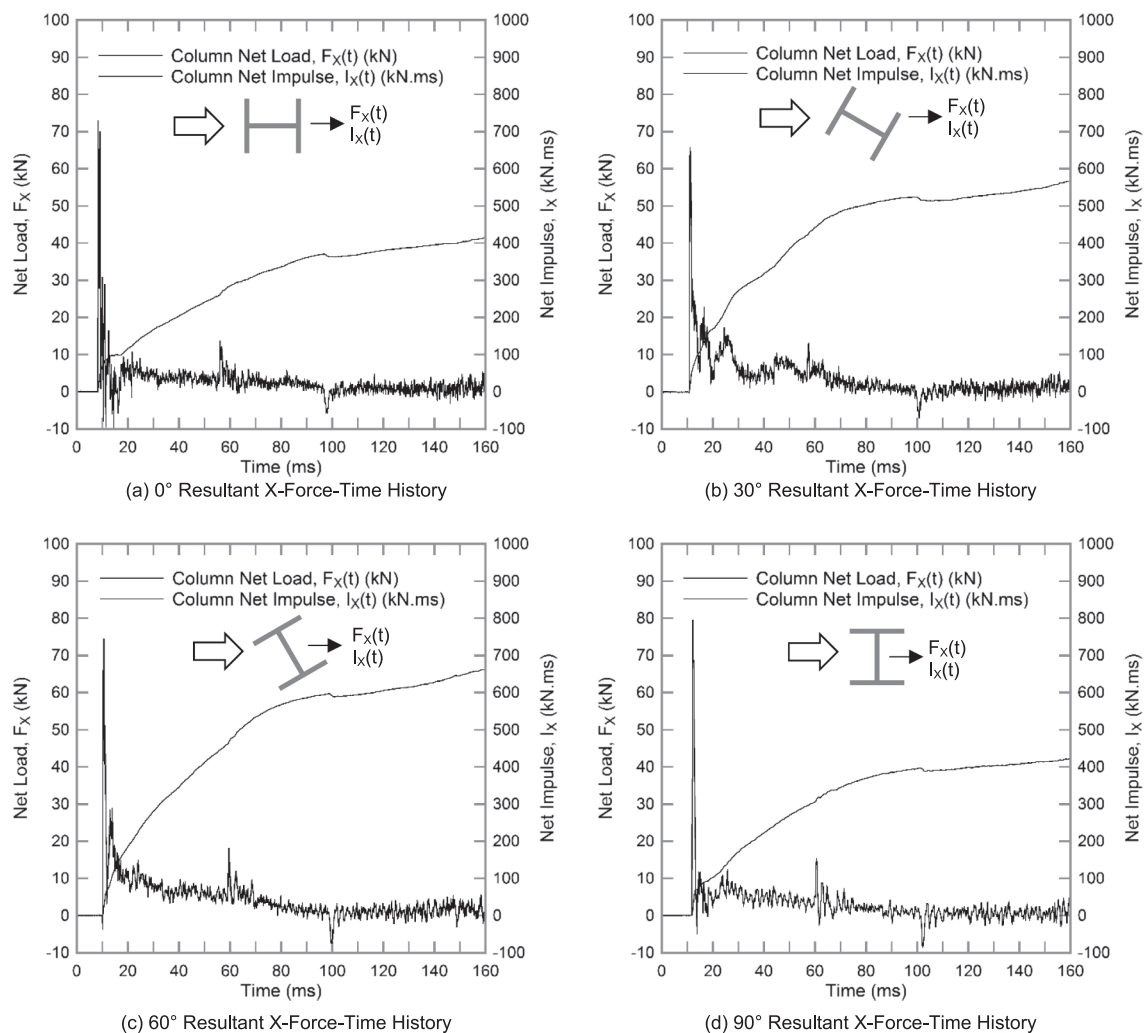
Fig. 9. Net force-time histories and cumulative impulse exerted on I-section in blast X-direction.
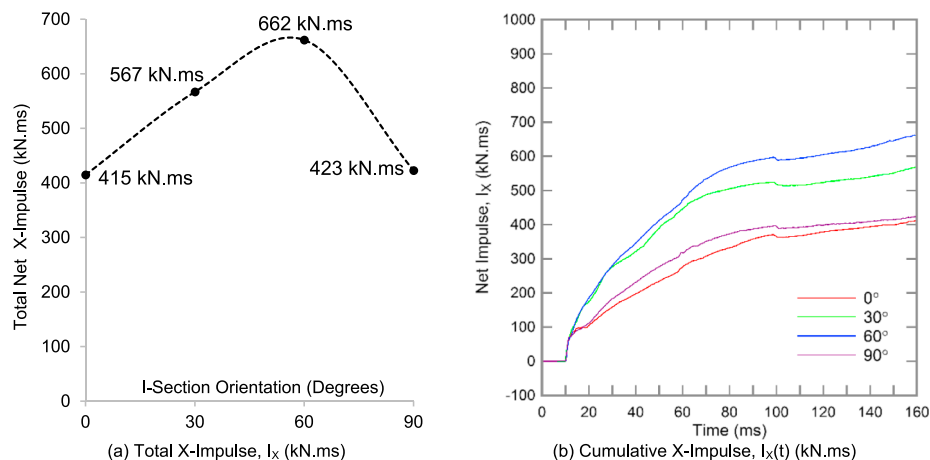

Fig. 10. Calculated net total and cumulative impulses exerted in X-direction on I-section at different orientations.

Using this approach, drag coefficients were calculated for the UKC $203 \times 203 \times 46$ I-section using the experimental dynamic incident impulse, column projected area and net total impulse calculated from respective surface pressure data as presented in Table 6. These drag coefficients assume rigid I-section response (no fluid-structure interaction) and take into account the column total projected area at different orientations, therefore encapsulating the influence of section

aerodynamics during blast drag loading.

Experimentally derived drag coefficients are plotted for each I-section orientation in Fig. 11, overlaid with proposed values from literature for comparison. Experimental drag coefficients varied with I-section orientation between $C_D = 1.82$–2.13 (Table 6). A drag coefficient of $C_D = 1.83$ was calculated for the 30° orientation, which is comparable to the I-section at orthogonal orientations of 0° or 90° despite the

Table 6
Experimentally calculated approximate drag coefficients for UKC 203 × 203 × 46 I-section.

I-section orientation	Incident dynamic impulse[a], I_q (kPa ms)	Total I-section projected area in X-direction, A_X (m^2)	Calculated total net X-impulse exerted on column, I_X (kN ms)	Calculated approximate drag coefficient, C_D
0°	380	0.600	415	**1.82**
30°	378	0.819	567	**1.83**
60°	379	0.819	662	**2.13**
90°	377	0.600	423	**1.87**

[a] This represents the total dynamic pressure impulse integrated over the positive phase duration consistent with the calculated net impulse exerted on the entire column, I_X.
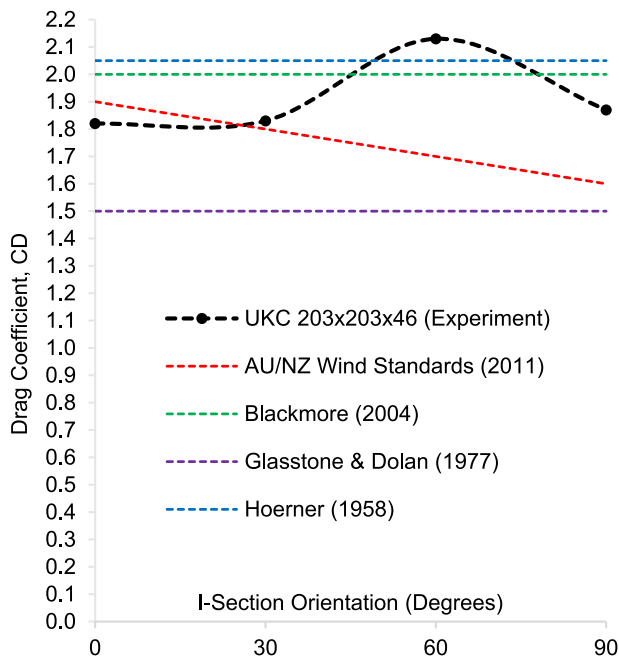

Fig. 11. Drag coefficients versus orientation compared with proposed values found in literature.

higher net impulse transfer (Fig. 10a). A noticeably higher drag coefficient of $C_D = 2.13$ is calculated for the 60° orientation, suggesting that maximum loading is caused by section aerodynamics. The 60° orientation exhibits a more pronounced increase in drag coefficient suggesting that multi-axis blast loading of an I-section does not exhibit symmetrical behaviour (Fig. 11). This also implies that it is not always accurate to employ a single drag coefficient modifier and rely on the changing projected area of the structural element.

Drag coefficients proposed in literature demonstrate varying levels of agreement to the I-section values calculated using experimental data (Fig. 11). Drag force coefficients proposed by The Australian & New Zealand Standards for Wind Actions [17] provide no guidance towards their applicability to intermediate orientations and therefore a linear variation was assumed with section orientation (Fig. 11). The experimentally-derived drag coefficient of $C_D = 1.82$ calculated for the 0° orientation falls slightly below (4%) the proposed AU/NZ Standards value of $C_D = 1.9$. At the 90° orientation, the experimentally derived drag coefficient ($C_D = 1.87$) exceeds the AU/NZ Standards proposed value of $C_D = 1.6$ by 17%. The drag coefficient proposed by Glasstone & Dolan [14] ($C_D = 1.5$) under-predicts the experimentally-derived coefficients for all orientations tested, thus providing an unreliable and potentially non-conservative prediction. For the 0, 30 and 90° orientations, drag coefficients proposed by Hoerner [15] and Blackmore [16] are conservative, being sufficiently greater than the experimental values calculated. At the 60° orientation however, the experimental drag coefficient ($C_D = 2.13$) exceeds all proposed values found in literature. Generally,

proposed values found in literature fail to describe the relatively high drag coefficient observed at oblique section orientations such as the 60° orientation. This suggests that proposed drag coefficients may only be reliable when applied about orthogonal I-section axes (i.e. 0° or 90°) and have potential to under-estimate blast loading.

3.2. Multi-axis structural response

For each trial and orientation tested, both I-section columns responded elastically. High-speed video capture of Specimen B (152 × 152 × 23 UKC section) was analysed to quantify maximum top deflection and examine the influence of multi-axis loading on column structural response. The camera position within the ABT enabled an elevation view of Specimen B's deflection in the tunnel downstream, X-direction (Fig. 12). Calibration of video footage was enabled by a marked scaling board held alongside the column top (Fig. 12a) and further verified by comparison of pixels with known column section dimensions. Multiple calibration tests demonstrated consistent agreement that 1 pixel represented 1.66 mm.

Peak column top displacements were calculated using two approaches utilising either background or foreground reference points to quantify the relative camera movement between the time of shockwave arrival and time of peak column deflection (Fig. 12c and d). Depending on I-section orientation, two or three reference points at the column top were tracked between blast arrival and at maximum deflection. Using these approaches, relative horizontal translation of the column top coordinates, DX_1, DX_2 and DX_3 were calculated (Fig. 12d). The average horizontal translation of these points, DX was calculated representing the peak column top deflection in the ABT downstream X-direction, as observed by the elevation camera view (Fig. 12b). Peak deflection, DX could not be decomposed into constituent column displacement vectors, x′ and y′ as this does not represent the true resultant displacement, R′ of the column (Fig. 12b). For oblique orientations, greater deflection about the weaker axis (y′ direction) will have occurred, therefore the resultant deflection of the section, R′ would not perfectly align with the global X-direction assumed for video analysis. The column will have displaced away or towards the camera in the y′ and x′ directions at oblique orientations, which may have introduced small parallax errors that undermine the pixel calibration performed. Notwithstanding, video analysis enabled acceptable quantification of I-section peak deflection as a function of orientation.

Upper and lower bound mean peak displacements, DX were calculated using both methods, either using background or foreground static reference points (Fig. 12c and d, Table 7). For both approaches, peak displacement calculations were made with ± 1.66 mm degree of accuracy, thus representing minimal uncertainty with a range of 3.3–8.8% of the measured displacements. The degree of agreement between upper and lower bound calculations was predominantly influenced by the degree of camera shake and reduced visibility caused by dust. Both methods generally calculated peak displacements with fair agreement within 8 mm on average.

Column specimens were recorded attaining peak deflection at a time t = 28–33 ms after shockwave arrival for all trials. The largest
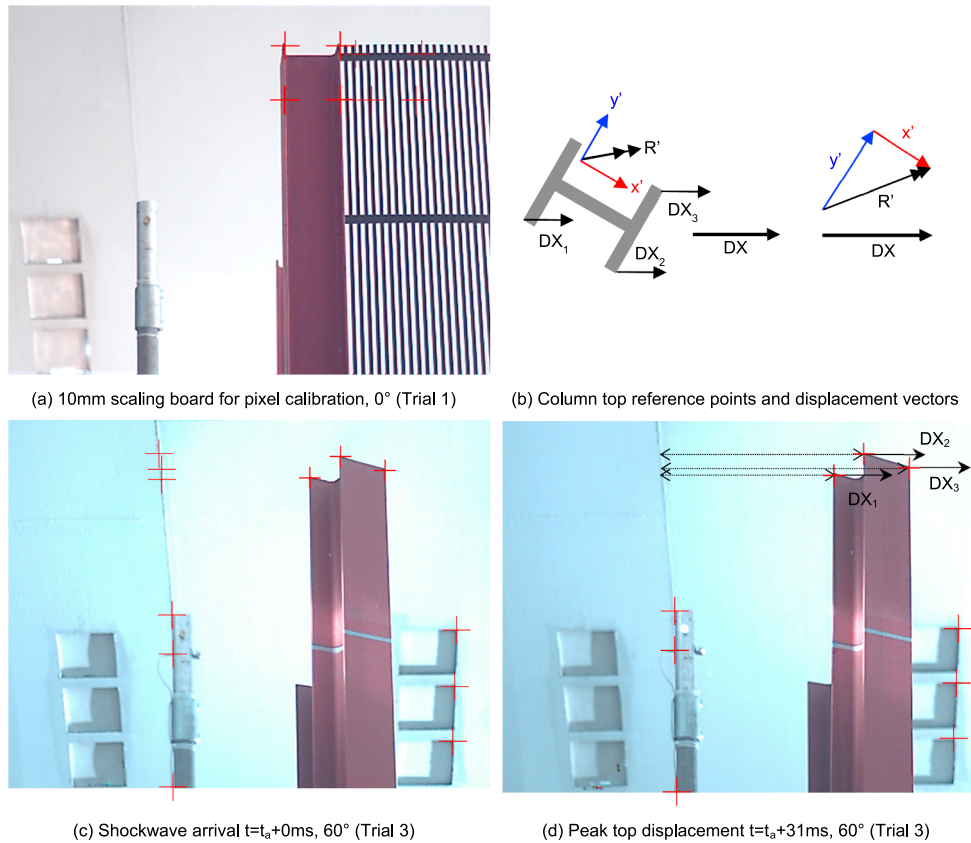
(a) 10mm scaling board for pixel calibration, 0° (Trial 1)

(b) Column top reference points and displacement vectors

(c) Shockwave arrival t=t_a+0ms, 60° (Trial 3)

(d) Peak top displacement t=t_a+31ms, 60° (Trial 3)

Fig. 12. High speed video analysis: scaling (a); static reference points (c, d); plan view schematic illustrating column top reference points and X-displacement, DX (b).

Table 7
Upper and lower bound mean peak top displacements of the UKC 152 × 152 × 23 column in the downstream X-direction calculated from high speed video analysis.

Trial	Section orientation	Top deflection, DX (mm)	
		Lower bound	Upper bound
1	0°	18	31
2	30°	43	47
3	60°	55	63
4	90°	42	49

deflection occurred for the 60° orientation with top X-displacement calculated as DX = 55–63 mm (Fig. 13). The 30° and 90° orientations exhibited the second largest peak deflections of 43–47 mm and 42–49 mm respectively. The 0° orientation showed the lowest displacement of DX = 18–31 mm. The 60° orientation recorded an upper bound X-displacement (DX = 63 mm) twice that of the upper bound 0° orientation displacement (DX = 31 mm). Considering the principal I-section axes, the 90° orientation lower bound top X-displacement (DX = 42 mm) was over twice that of the lower bound measurement for the 0° orientation (DX = 18 mm). Despite similar total impulses exerted on the column at both 0° and 90° orientations, deflection at the 90° orientation was over double that of the 0° orientation (Fig. 14).

These experimental results demonstrate that while the section orientation influences the blast drag loading exerted on the column, structural response is also influenced by the mechanical flexural properties of the section. The second moment of area of Specimen B about the weaker axis is approximately a third of the major axis (Table 2), which explains the larger deflection observed at 90°. It has been shown that structural blast response of an I-section column subjected to multi-axis long-duration blast loads is therefore governed by section

mechanical flexural properties and net blast drag loading, both of which are a function of the I-section orientation. For elastically deforming columns, these results demonstrate that multi-axis blast loading on I-section columns has a significant effect on structural response in terms of peak transient deflection.

4. Conclusions

This paper has presented new experimental results from four full-scale blast trials that investigated the multi-axis response of steel I-section columns to long-duration blast loading. Successful data capture of specific column surface impulses quantified multi-axis blast interaction and aerodynamic effects as a function of I-section orientation. Variation of surface impulses with I-section orientation demonstrated the influence of surface exposure to the blast and the presence of aerodynamic effects; flow separation, regions of wake and vorticity reduced the total impulse exerted on less-exposed or entirely shielded surfaces. Oblique I-section column orientations were observed to exert larger net total impulses with a maximum observed at 60°. Experimental drag coefficients were calculated for each I-section orientation tested. It was found that drag coefficients proposed in literature have the potential to under-predict drag loading for certain oblique I-section orientations such as the 60° orientation examined in these experiments. Results provide reason to question the accuracy of proposed drag coefficients in literature for blast drag problems when oblique-axis interaction is concerned.

Analysis of high-speed video footage enabled calculation of the column peak downstream deflection. Maximum deflection was observed for the 60° I-section orientation, approximately three times greater than the 0° orientation, demonstrating that multi-axis blast loading has a significant effect on the magnitude of structural response. It was shown that long-duration blast response of I-section columns is governed by net blast drag loading and section mechanical properties,
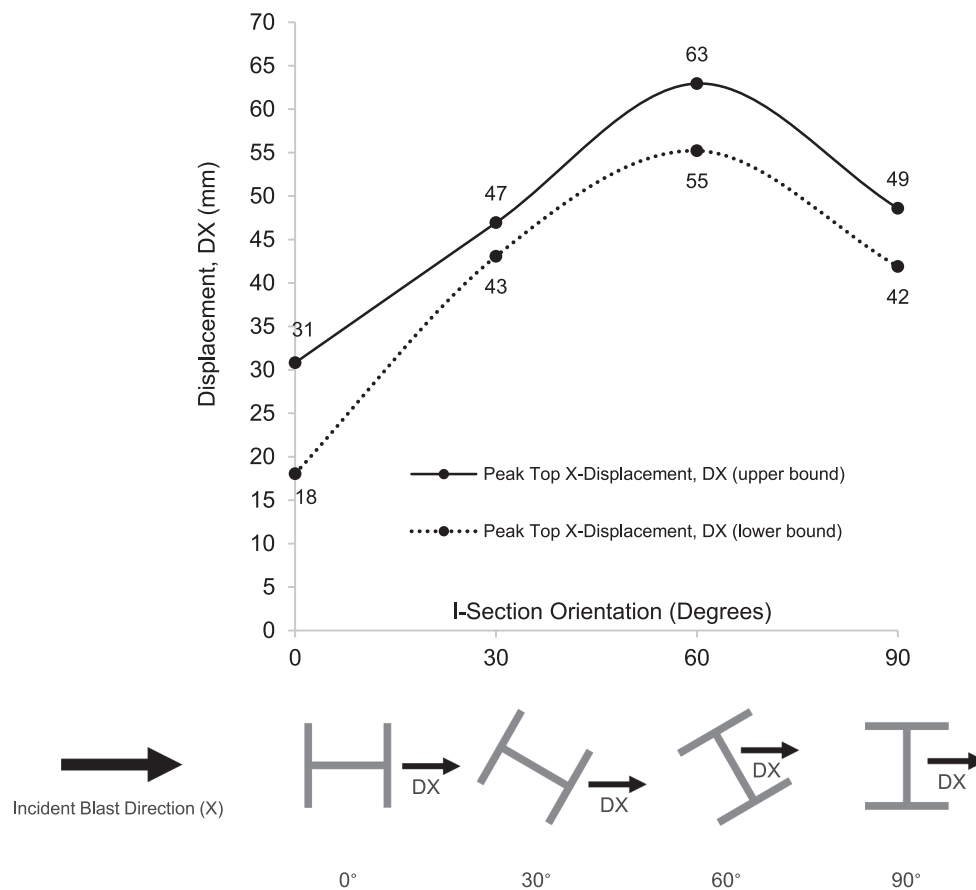
Fig. 13. Specimen B (UKC 152 × 152 × 23) peak top X-displacement, DX.

(a) Net total impulse exerted in X-direction, I_x.

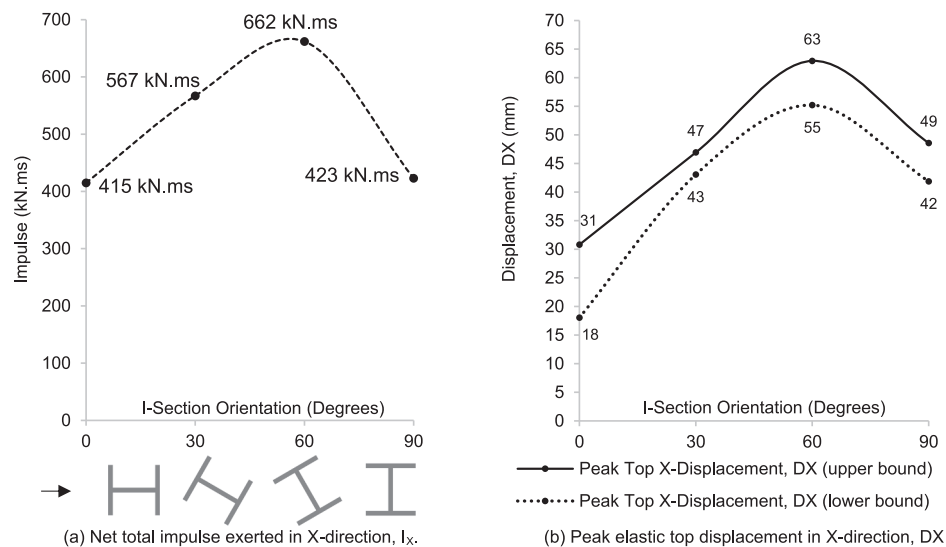(b) Peak elastic top displacement in X-direction, DX

Fig. 14. Resultant total impulse exerted on Specimen B and resulting peak top displacement in the X-direction.

both of which are directly related to I-section orientation. Overall, results from this experimental work have confirmed that I-section columns are axis-sensitive to blast wave direction giving rise to varying magnitudes of drag loading and resulting structural response.

Acknowledgements

References

[1] Steel Construction Institute. Buncefield explosion mechanism phase 1, vols. 1 and 2. Ascot; 2009.

[2] Atkinson G, Cusco L. Buncefield: a violent, episodic vapour cloud explosion. Process Saf Environ Prot 2011;89(6):360–70.

[3] Atkinson G. Blast damage to storage tanks and steel clad buildings. Process Saf Environ Prot 2011;89(6):382–90.

[4] U.S. Chemical Safety Board. Preliminary findings into the west fertilizer explosion and fire; 2013.

[5] Huang Z, Dai K, Wang J, Wu HF. Investigations of structural damage caused by the fertilizer plant explosion at west, Texas. I: air-blast incident overpressure. J Perform Constr Facil 2016;30(4).

[6] Edmunds JE, Wiehle CK, Kaplan K. Structural debris caused by nuclear blast (URS 639-4). Washington, D.C.; 1964.

[7] Mays G, Smith P, editors. Blast effects on buildings. 1st ed.Thomas Telford Limited; 1995.

[8] US Department of Defense (DoD). UFC 3-340-02, 'Structures To Resist The Effects Of Accidental Explosions.' Washington, D.C.; 2008.

[9] Krauthammer T. Modern protective structures; 2008.

[10] Smith PD, Hetherington JG. Blast and ballistic loading of structures; 1994.

[11] Shi Y, Hao H, Li Z-X. Numerical simulation of blast wave interaction with structure columns. Shock Waves 2007;17:113–33.

[12] Rigby SE, et al. A numerical investigation of blast loading and clearing on small targets. Int J Prot Struct 2014;5(3).

[13] Ballantyne GJ, Whittaker AS, Dargush GF, Aref AJ. Air-blast effects on structural shapes of finite width. J Struct Eng 2010;136(February):152–9.

[14] Glasstone S, Dolan PJ. The effects of nuclear weapons, 3rd ed. United States Department Of Defense and the Energy Research and Development Administration; 1977.

[15] Hoerner SF. Fluid dynamic drag; 1958.

[16] Blackmore P, editor. Wind loads on unclad structures (BRE). BRE Electronic Publications; 2004.

[17] Standards Australia Limited/Standards New Zealand. AS-NZS 1170.2:2011, 'Structural Design Actions – Part 2: Wind actions; 2011.

[18] Kingery CN, Bulmash G. Airblast parameters from tnt spherical air burst and hemispherical surface burst' Technical Report ARBRL-TR-02555; 1984.

[19] Clubley SK. Non-linear long duration blast loading of cylindrical shell structures. Eng Struct Feb. 2013;59:113–26.

[20] Clough L. Synergistic response of steel structures to thermal and blast loading. University of Southampton; 2016.